Enhanced Inertia Response Control of Grid-forming PMSG-based Wind Turbines Considering Safe Operation Boundary

Zhenyan Deng, *Student Member*, *IEEE*, Han Wang, *Member*, *IEEE*, Yao Qin, *Graduate Student Member*, *IEEE*, Renxin Yang, *Member*, *IEEE*, and Xu Cai, *Senior Member*, *IEEE*

***Abstract*—With the rapid development of renewable energy, power system inertia is gradually decreasing, threatening the stability of system frequency. Grid-forming (GF)-based wind turbines (WTs) equipped with active inertia response are key to addressing the problem of low-inertia power systems. However, existing researches have focused on the inertia response of GF-based WTs in the maximum power point tracking (MPPT) range, while lacking the discussion on the control and implementation of inertia response in other operating ranges. Therefore, this paper proposes an inertia response control method for permanent magnet synchronous generator (PMSG)-based WTs across the full wind speed range based on inertia synchronization control (IsynC). By analyzing the characteristics of the inertia response and safe operating boundaries of the WT at different operational stages, a control method for the smooth speed transition of the WT across different operating ranges is proposed. By utilizing a composite judgment logic based on the DC voltage rate of change and rotor speed, an adaptive inertia response for different operating modes is achieved. Single and multiple PMSG-WT simulation models are built in PSCAD/EMTDC to simulate the proposed full wind speed range inertia response control and its operational characteristics. The results demonstrate that this method enables the selective inertia response of WTs across the full wind speed range, effectively enhancing the frequency support capabilities of renewable energy generation systems.**

***Index Terms*—Grid-forming, permanent magnet synchronous generator (PMSG), inertia response, full wind range, seamless switching.**

I. Introduction

With China's efforts to advance toward its "emission peak" and "carbon neutrality" targets, the integration of renewable energy into the grid has been steadily increasing. As a result, traditional power systems now prominently feature a combination of high proportion of renewable energy sources and widespread use of power electronic devices [1], [2]. Currently, renewable energy generation units, particularly wind and solar units, neither provide inherent inertia to the grid nor offer active frequency support [3]. This leads to a consistent decline in the system's overall inertia, manifesting a trend of diminished resilience or "weakening" [4], [5]. This evolving landscape poses significant challenges to the safe and stable operation of power systems.

Numerous studies have been conducted on wind turbines (WTs) participating in power system frequency regulation. These primarily encompass the followings:

1) A portion of the active power of the WTs is reserved for grid frequency modulation. By deviating WTs from the maximum power point tracking (MPPT) curve and deliberately increasing the pitch angle to reserve power, the WTs can be used to respond to grid frequency variations [6]. However, this method reduces the responsive power of WTs when the system frequency increases.

2) Introduction of the rate of change of frequency (RoCoF) into the control loop enables the establishment of a dynamic relationship between grid frequency and WTs' output power to realize inertia response [7]–[10].

3) Configuration of energy storage devices to enhance the frequency response capability of WTs [11], [12].

4) Utilization of grid-forming (GF) control, which allows autonomous synchronization to the grid without phase-locked loop (PLL) and provides the capability to actively support grid frequency.

In [13], a control method combining active power-frequency (P-f) droop and reactive power-voltage (Q-V) droop is proposed, enabling grid-tied inverters to emulate the output characteristics of a synchronous

Received: September 26, 2024
Accepted: May 15, 2025
Published Online: September 1, 2025
Zhenyan Deng, Han Wang (corresponding author), Yao Qin, Renxin Yang, and Xu Cai are with the Laboratory of Control of Power Transmission and Conversion, Shanghai Jiao Tong University, Shanghai 200240, China (e-mail: dengzy@sjtu.edu.cn; wanghansjtu@sjtu.edu.cn; qy_dawn@sjtu.edu.cn; frank_yang@sjtu.edu.cn; xucai@sjtu.edu.cn).
DOI: 10.23919/PCMP.2023.000153

generator (SG). In [14] and [15], virtual synchronous generator (VSG) control is introduced, allowing the inertia and damping characteristics of a grid-tied converter. However, although its output characteristics are more akin to those of an SG, it cannot be directly applied to a WT that requires DC voltage control. For high voltage direct current (HVDC) converters, a power-synchronization control method is proposed in [16], in which the output of the DC voltage controller serves as the active power reference. By integrating the deviation of the active power, the grid angle is derived, enabling the converter to synchronize autonomously with the grid without phase locking and to emulate the characteristics of SG. However, the synchronization mechanism of this method is relatively complex. In [17], a control method is proposed based on the dynamic characteristics of the DC capacitor of a wind power converter to autonomously achieve grid synchronization. It possesses the inertia response characteristics of SG and allows doubly-fed WTs to autonomously sense the grid frequency and perform inertia response. This autonomous GF control method is also termed inertia synchronization control (IsynC). Subsequently, references [18]–[20] apply this autonomous control method to flexible DC transmission systems and WTs based on permanent magnet synchronous generator (PMSG). The researches indicate that IsynC can be applied to various units in the renewable energy field, demonstrating its strong applicability.

While references [17]–[20] provide a detailed discussion of the principles of IsynC and its application in various wind power generation systems, their researches are limited to the MPPT stage. They do not address control methods under real full-wind range conditions, where the WTs operate at varying speed and different power pitch most of the time. As a result, the operational range for the inertia response is severely constrained, reducing the effectiveness of WTs in supporting the grid frequency. Therefore, the pressing issues include how to achieve full wind range inertia response control for GF-controlled WTs, how to evaluate the inertia response performance of WTs, and how to define a stable operating range.

Current researches on the operational control of WTs are predominantly focused on the MPPT mode, with less emphasis on the control strategies across the entire wind speed range. In [21], a strategy involving control loop switching is presented, where torque control is applied during the MPPT mode which is shifted to speed control under high wind speed conditions. Demagnetization control, which explores the maximization of PMSG electromagnetic torque at high wind speed, is proposed in [22] and is categorized as direct torque control. However, it does not address speed control under high wind conditions. Some studies have suggested to generate optimal torque command based on wind speed lookup table at low wind speed, with high wind speed control managed by pitch control [23]–[25]. A main controller is employed to issue power/torque commands, and once the rotor speed reaches the rated value, the torque command is limited to prevent further increase in the speed. However, the aforementioned approaches differ from the commonly used approach in commercial WTs. In [26]–[29], the torque/power commands for the system are defined according to the different speed ranges of the WT. A segmented function approach is used, which actively reduces the part of the load under high wind speed to prevent over speeding.

In this paper, IsynC-based WTs are enhanced, culminating in the proposal of a comprehensive inertia response control methodology tailored for them. This approach ensures that WTs are equipped with inertia response capabilities across all operation modes: low constant speed, MPPT, high constant speed, and constant power mode. An in-depth examination of the inertia response characteristics, safe operating boundaries, and control methods of the WTs throughout the entire wind speed range is conducted. The results indicate an enhanced inertia response capacity of the WTs. Notably, the introduced methodology allows for flexible and seamless transitions between different operational stages. A detailed model of a PMSG-WT unit is constructed in PSCAD/EMTDC, alongside a grid model consisting of one hundred IsynC-based WTs. Simulations subsequently confirm the efficacy of the control method presented herein.

The remainder of this paper is organized as follows. Section II presents the basic technical route of WT based on IsynC. Section III proposes an enhanced inertia response control across the full wind speed range. Section IV demonstrates the simulation results of a single WT and wind farm based on PSCAD/EMTDC after adopting the proposed strategy. Finally, the conclusion of this paper is addressed in Section V.

II. Technical Routes of the IsynC-based WT

The schematic structure of the wind power system is illustrated in Fig. 1. It encompasses a WT, a PMSG, a machine-side converter (MSC), a grid-side converter (GSC), a LC filter, and a transformer. In Fig. 1, C_{dc} represents the DC capacitor; while L_f and C_f denote the inductance and capacitance of the filter, respectively; L_g is the grid equivalent inductance; U_{dc} is the DC voltage; while ω_r and θ_r correspond to the rotor angular speed and rotor angle, respectively; U_{sabc} and I_{sabc} represent the three-phase voltage and current outputs of the generator, respectively; U_{pabc} is the voltage at the grid connection point; I_{tabc} is the output current of the WT; while S_m and S_g correspond to the control signals for the MSC and GSC, respectively.

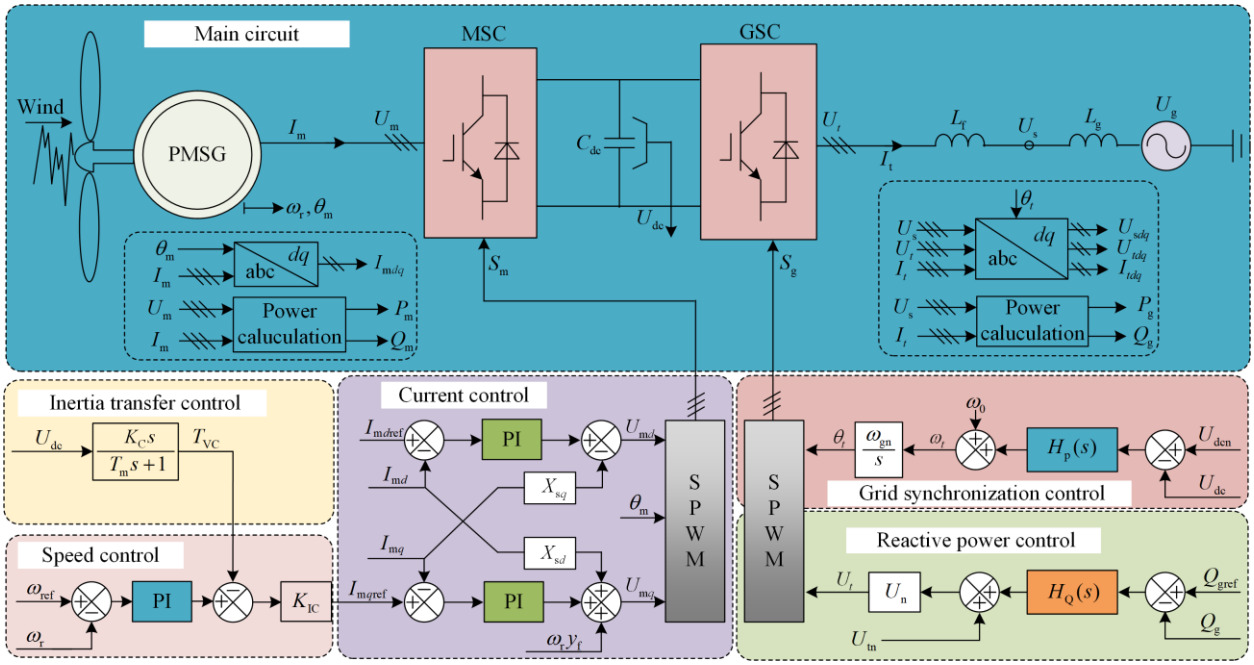

Fig. 1. System structure and control block diagram of an IsynC-based WT.

A. Self-synchronization Principle of GSCs

The GSC is synchronized with the grid using the inertia of the DC capacitor. The difference between the set and the actual values of u_{dc} is fed into the grid synchronization controller $H_p(s)$ to obtain the angular frequency of the AC voltage output of the GSC, whereas its integration yields the phase angle θ_t of the AC voltage output. This process can be represented as:

$$\begin{cases} \omega_t = (u_{dcn} - u_{dc})H_p(s) + \omega_0 \\ \theta_t = \omega_{gn}\int \omega_t \mathrm{d}t \end{cases} \tag{1}$$

where ω_0 and ω_{gn} represent the initial and rated values of the grid frequency, respectively; u_{dcn} denotes the rated value of the DC voltage; s denotes the differential operator; and $H_p(s) = K_{\theta P}$ ($K_{\theta P}$ is the proportional coefficient of the grid synchronization controller).

From the GSC control block diagram of the WT based on IsynC shown in Fig. 1, the magnitude U_t of the output voltage from the WT's GSC can be expressed as:

$$U_t = \left[(Q_{gref} - Q_g)H_Q(s) + U_{tn}\right]U_N \tag{2}$$

where U_{tn} represents the rated magnitude of the grid voltage; $H_Q(s) = K_{QP} + K_{QI}/s$ denotes the reactive power controller (K_{QP} and K_{QI} are the PI coefficients of the controller); Q_{gref} and Q_g correspond to the set and rated values of the reactive power output, respectively; while U_N is the base voltage.

The IsynC-based WT directly controls the amplitude and phase of the output voltage of the GSC, exhibiting the characteristics of a controlled voltage source.

B. Inertia Transfer Control of the MSC

Compared to the MSC with traditional vector control, only an inertia transfer control loop needs be added when utilizing the inertia of the DC capacitor for synchronization. The current control loop can be described as:

$$\begin{cases} U_{sd} = (K_{pi} + \dfrac{K_{ii}}{s})(I_{sdref} - I_{sd}) - I_{sq}X_{sq} \\ U_{sq} = \omega_e\psi_f + (K_{pi} + \dfrac{K_{ii}}{s})(I_{sqref} - I_{sq}) + I_{sd}X_{sd} \end{cases} \tag{3}$$

where I_{sdref} and I_{sd} represent the set and real values of the d-axis current of the PMSG, respectively; similarly, I_{sqref} and I_{sq} are the set and real values of the q-axis current of the PMSG, respectively; K_{pi} and K_{ii} denote the proportional and integral coefficients of the current controller, respectively; X_{sd} and X_{sq} are the dq-axis reactance of the generator; ω_e is the electrical angular speed of the generator; while ψ_f is the amplitude of the flux linkage.

The MSC controls the speed of the PMSG, where the speed setpoint is generated by the MPPT module. The difference between the set value and the actual speed is processed by a PI regulator to determine the d-axis current value, while the q-axis current command value is set to 0. The expression can be presented as:

$$\begin{cases} I_{sdref} = 0 \\ I_{sqref} = \left(\left(K_{po} + \dfrac{K_{io}}{s}\right)(\omega_{rref} - \omega_r) - T_{VC}\right)K_{IC} \end{cases} \tag{4}$$

where ω_{rref} denote the set speed of the rotor, respectively; K_{po} and K_{io} represent the proportional and integral coefficients of the speed controller, respectively; T_{VC} stands for the torque component of the inertia transfer control; and K_{IC} is the conversion coefficient from torque to current.

u_{dc} of the IsynC-WT can dynamically reflect the

changes in the grid frequency. By incorporating an additional inertia transfer control loop and integrating its output into the torque setpoint of the PMSG, it becomes feasible to effectively utilize the rotor inertia of the WT, thereby achieving an enhanced inertia response of the WT. This paper uses an additional torque approach to realize the inertia response of the IsynC-based WT system. Consequently, T_{VC} can be expressed as:

$$T_{VC} = u_{dc} \frac{K_C s}{T_m s + 1} \tag{5}$$

where T_m is the time constant of the inertia transfer loop and K_C is its coefficient.

III. Enhanced Inertia Response Control for Full Wind Range

For the inherent physical characteristics of WT systems, different control objectives are necessary across varying wind speed ranges. This paper introduces a method for the inertia response control targeting IsynC-based WT systems in the full wind speed range, which includes a seamless speed transition control unit for PMSGs and an adaptive inertia transfer control unit.

A. Operating Range of the IsynC-based WT

The operational speed range of the WT is constrained by the maximum safe speed ω_{max} and the minimum safe speed ω_{min}. As depicted in Fig. 2, when the wind speed v_w increases, the system operates in the following phases:

1) For v_w in (v_{in}, v_1), the system is in the constant low-speed phase (Phase I);

2) v_w lies in (v_1, v_2) and it corresponds to the MPPT phase (Phase II);

3) For v_w in (v_2, v_n), the system enters the constant high-speed phase (Phase III);

4) For v_w in (v_n, v_{out}), the operation enters the constant power phase (Phase IV).

Herein, v_{in} is the cut-in wind speed; v_1 is the wind speed entering the MPPT phase; v_2 is the wind speed transitioning to the constant speed phase; and v_{out} is the cut-out wind speed.

Figure 2 shows that when v_w falls within the range of (v_1, v_{11}) and (v_{21}, v_2), the turbine operates in the transition regions between the low constant speed and MPPT phases, and between the MPPT and high constant speed phases, respectively. To streamline the analysis, this paper considers both intervals as operating under the MPPT mode [30].

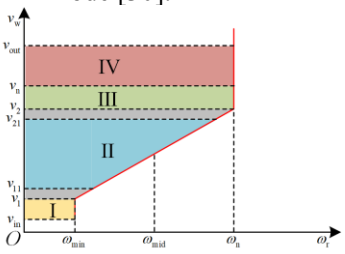

Fig. 2. Operating state diagram of the WTs in the full wind speed range.

B. Seamless Speed Transition Control of the WT

Figure 3 illustrates the speed control unit proposed in this paper for the full wind speed range, which includes a low wind speed controller, a high wind speed controller, and a multipath selector controller. Here, ω_n corresponds to the rated speed and ω_{rmid} is the intermediate speed utilized for switching controls under different wind speed ranges.

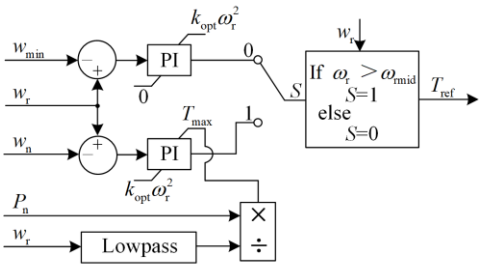

Fig. 3. Control structure of seamless speed transition control of PMSG.

The maximum and minimum torque limits, T_{e1H} and T_{e1L}, of the output torque T_{e1} from the speed controller in the low wind speed range are given by:

$$\begin{cases} T_{e1H} = k_{opt}\omega_r^2 \\ T_{e1L} = 0 \end{cases} \tag{6}$$

where k_{opt} represents the coefficient for maximum wind power tracking.

The maximum and minimum torque limits, T_{e2H} and T_{e2L}, of the output torque T_{e2} from the speed controller in the high wind speed range are:

$$\begin{cases} T_{e2H} = T_{max} \\ T_{e2L} = k_{opt}\omega_r^2 \end{cases} \tag{7}$$

where T_{max} represents the maximum torque of the generator.

The operation of the WT under different rotor speed can be described as follows.

1) When ω_r is less than ω_{min}, the torque setpoint of the WT is determined by the output of the speed controller in the low wind speed range. As shown in Fig. 3, because ω_r is less than ω_{min}, the T_{eref} setpoint of the WT unit produced by the PI controller is equal to the minimum torque amplitude of 0. Thus, the power output of the WT is 0, and the WT operates in a constant low-speed operating mode.

2) When ω_r is greater than ω_{min} but less than ω_{rmid}, the torque setpoint is again determined by the output of the speed controller in the low wind speed range. When ω_r is greater than ω_{min}, T_{eref} is equal to the maximum torque limit $k_{opt}\omega_r^2$. At this stage, the wind turbine operates in the MPPT mode.

3) When the rotational speed ω_r is greater than ω_{rmid} but less than the rated speed ω_n, the torque setpoint is determined by the output of the speed controller in the

high wind speed range. When ω_r is less than ω_n, T_{eref} is equal to the minimum torque limit $k_{opt}\omega_r^2$. During this period, the WT also operates in the MPPT mode.

4) When the rotational speed ω_r exceeds ω_n, the torque setpoint is determined by the output of the speed controller in the high wind speed range. When the WT's output torque is equal to T_{emax}, the WT operates in the constant high speed operation phase. If the WT's output torque exceeds T_{emax}, the torque of the WT unit surpasses ω_n, and the pitch controller is activated to reduce the wind power captured by the WT. During this time, the WT operates in the constant power operation phase.

Typically, ω_{min} is set to 60% of ω_n, and ω_{rmid} is set to 80% of ω_n. The seamless speed transition control method proposed in this paper has the following characteristics.

1) The PI regulators of both the low wind speed range controller and the high wind speed range controller operate in the near saturation state.

2) The upper limit of the torque output from the low wind speed range is equal to the lower limit of the torque output from the high wind speed range.

3) The switch value ω_{rmid} of the speed controller is set at the midpoint between the minimum speed ω_{min} and the rated speed ω_n.

These features allow the speed variation of the WT to automatically switch between the four operating phases. During the transition of the speed controller, the desaturation effect of the PI regulator can be utilized to achieve seamless and flexible transitions between different operational intervals. This method circumvents the gradient issues associated with the lookup table method and preserves the operational interval of the unit's MPPT to the greatest extent [31].

C. Adaptive Inertia Response Control in a Full Wind Range

As shown in Fig. 2, in range I, the output power of the WT is minimal, and its speed is controlled at the lowest operating speed. As a result, it cannot release the rotor's kinetic energy and thus has no inertia response capability when the grid frequency drops. In this mode, the input command value for the current controller is given by:

$$I_{sd\text{ref1}} = \begin{cases} (T_{e1L} + T_{VC})K_{IC}, & (su_{dc} > 0) \\ T_{e1L}K_{IC}, & (su_{dc} < 0) \end{cases} \tag{8}$$

The rotor kinetic energy E_{VC} released by the WT generator during the inertia response is defined as:

$$E_{VC} = \int_0^{t_{inr}} P_{VC}\mathrm{d}t = \int_0^{t_{inr}} \frac{K_C S_n}{f_{gn}} \mathrm{e}^{-\frac{t}{T_m}}\mathrm{d}t \approx \frac{t_{inr}K_C S_n}{f_{gn}} \tag{9}$$

where t_{inr} is the duration of the inertia response and P_{VC} is the power from the inertia transfer portion; S_n is the rated power; and f_{gn} is the rated frequency of the grid. At this point, the WT generator absorbs power, and the energy boundary that slows the system frequency variation is described by:

$$E_{VC} \leqslant \Delta E_{max1} = \left|\frac{1}{2}J(\omega_{max}^2 - \omega_{r0}^2)\right| \tag{10}$$

where ΔE_{max1} is the maximum kinetic energy that can be released by the rotor of the WT generator at a constant low speed; ω_{max} and ω_{r0} are the maximum allowable and current rotary speeds, respectively.

Similarly, in phase II, the WT operates in the MPPT mode. At this time, the rotor speed can increase or decrease, allowing the WT to respond to grid frequency increase or decrease. The input command value for the current controller during this phase is given by:

$$I_{sd\text{ref2}} = \begin{cases} (k_{opt}\omega_r^2 + T_{VC})K_{IC}, & (su_{dc} > 0) \\ (k_{opt}\omega_r^2 + T_{VC})K_{IC}, & (su_{dc} < 0) \end{cases} \tag{11}$$

During this phase, the energy boundary of the WT generator used for the inertia response is given by:

$$\begin{cases} E_{VC} \leqslant \Delta E_{max\,21} = \left|\frac{1}{2}J(\omega_{max}^2 - \omega_{r0}^2)\right| \\ E_{VC} \leqslant \Delta E_{max\,22} = \left|\frac{1}{2}J(\omega_{r0}^2 - \omega_{min}^2)\right| \end{cases} \tag{12}$$

In phase III, the rotor speed reaches its rated value. At this time, the WT can release rotor kinetic energy to support the transient frequency drop in the grid. However, the inertia response to the system frequency increase may cause the speed to exceed its bounds due to the reduction in the output of the WT. Therefore, during this phase, the WT does not respond to frequency rise events caused by load shedding. The input command value for the current controller during this stage is given by:

$$I_{sd\text{ref3}} = \begin{cases} (T_{e2H} + T_{VC})K_{IC}, & su_{dc} > 0 \\ (T_{e2H} + T_{VC})K_{IC}, & su_{dc} < 0 \end{cases} \tag{13}$$

The inertia response boundary during this stage is given by:

$$E_{VC} \leqslant \Delta E_{max\,3} = \left|\frac{1}{2}J(\omega_{r0}^2 - \omega_{min}^2)\right| \tag{14}$$

In phase IV, since the output power of the WT has reached its rated value, the increased output power that can be achieved by the unit's inertia response to a drop in grid frequency is limited, making inertia response unfeasible. During this stage, the inertia response control capability of the WT generator should be limited according to changes in the grid frequency, that is:

$$I_{sd\text{ref3}} = I_{sd\text{ref4}} \tag{15}$$

In the constant power operation mode, the boundary of the inertia response is the same as that in the constant high speed mode:

$$E_{VC} \leqslant \Delta E_{max\,4} = \Delta E_{max\,3} \tag{16}$$

Based on the above considerations, this paper proposes an adaptive inertia response control method for the full wind speed range. It can respond "selectively"

to grid frequency variations based on the current operating state of the WT and protection requirements. This achieves inertia response capabilities throughout the wind speed range, with its output expressed as:

$$T_{VC} = S_{VC}(u_{dc}, \omega_r) G_{VC}(s) s u_{dc} \tag{17}$$

where $S_{VC}(u_{dc}, \omega_r)$ is defined as the inertia response selection function, which is a binary function in terms of u_{dc} and ω_r; $G_{VC}(s)$ is the low-pass filter in Eq. (5).

Figure 4 presents the framework of the adaptive inertia response control. Based on the rate of change in u_{dc} and ω_r, the grid frequency variation and the wind speed range in which the WT operates are instantly identified. By outputting 0/1 signals, the enabling and blocking of the inertia response capability are realized.

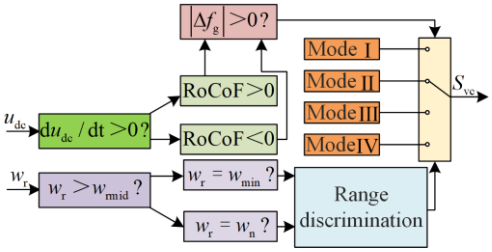

Fig. 4. Adaptive inertia response schematic.

With the inclusion of the adaptive inertia transfer control module, the input value of the current control loop can be expressed as:

$$I_{sdref} = (T_{eref} + S_{VC}(u_{dc}, \omega_r) G_{VC}(s) s u_{dc}) K_{IC} \tag{18}$$

where T_{eref} is the output of the speed PI controller. According to Eq. (18), with the addition of adaptive inertia transfer control, the IsynC-based WT can autonomously respond to frequency change based on the rate of change of u_{dc} across the full wind speed range. It selectively releases/stores rotor kinetic energy based on the real-time operating state of the WT, so as to support the system frequency. This realizes a holistic control strategy for the WT, addressing both frontend protection and direct speed control.

IV. Simulation Verification

First, an IsynC-based WT is selected and is subjected to a fixed grid frequency variation and four wind speeds corresponding to different phases. The seamless speed switching control strategy for the full wind speed range proposed in this paper, as well as the adaptive inertia response function, are then verified. In the second step, a wind farm comprising 100 IsynC-based WTs is set up in the grid model. This includes WT groups operating at different wind speeds to verify the enhancement effect of the control strategy proposed in this paper when multiple units are running in parallel. The WT electrical and mechanical parameters are shown in Tables I and II, respectively.

TABLE I
Electrical Parameters of a Full-power Wind Turbine

Symbol	Description	Value
S_N(MW)	Rated power	2.0
U_N(kV)	Rated value of AC voltage	0.69
u_{dcn}(kV)	Rated value of DC voltage	1.2
C_{dc}(mF)	DC-link capacitor	32.76
L_f(μH)	Filter inductance	160
C_f(μH)	Filter capacitor	600
f_N(Hz)	Rated frequency of PMSG	9.75
H_{wt}(s)	Inertia time constant of PMSG	4.0
L_s(mH)	Synchronous inductance	5.12
f_{ms}(Hz)	Switching frequency of MSC	2000
f_{gs}(Hz)	Switching frequency of GSC	3000

TABLE II
Mechanical Parameters of the Wind Turbine

Symbol	Description	Value
R_A(m)	Rotor radius	60.5
v_{in}(m/s)	Cut-in wind speed	2.5
v_n(m/s)	Rated wind speed	9
v_{out}(m/s)	Cut-out wind speed	25
λ	Optimal tip speed ratio	11
J_w (kg·m^2)	Rotational inertia of turbine	3.134×10^7

A. Verification of Seamless Speed Transition Control

The simulation conditions are as follows. At $t = 15$ s, the wind speed v_w jumps from 6 m/s to 10 m/s, transitioning the WT from the MPPT operating phase to the constant power operating phase. At $t = 25$ s, v_w drops to 6 m/s, causing the WT to transition from the constant-power operating phase back to the MPPT operating phase. The corresponding simulation waveforms are shown in Fig. 5(a).

From Fig. 5(a), it is evident that prior to $t = 15$ s, the rotor speed ω_r is 0.85 p.u. and the unit's output active power P_g is 0.55 p.u., operating in the MPPT phase. After v_w jumps to 10 m/s, ω_r starts to increase. By $t = 16$ s, P_g climbs to 1.0 p.u., and the pitch control mechanism is then activated. The pitch angle β gradually increases from 0° to 1.5°. At this point, the output power is constrained at 1 p.u., and the WT operates in the constant power phase. At $t = 25$ s, when v_w drops to 6 m/s, ω_r, P_g, and β revert to their respective values before the wind speed change. Throughout the process, u_{dc} is maintained at its rated value, and is consistent with the grid frequency f_g. The simulation results demonstrate that during a step change in wind speed, the proposed full wind speed range speed control strategy can achieve smooth control of the rotor speed and seamlessly transition between the MPPT, constant

speed, and constant power operating phases.

To further validate the effectiveness of the control strategy proposed in this paper, another simulation is set up where the wind speed changes from 3 m/s to 10 m/s at a certain slope. In this scenario, the IsynC-based WT sequentially operates in constant low-speed mode (I), MPPT mode (II), constant high-speed mode (III), and constant-power mode (IV). The corresponding simulation waveforms are shown in Fig. 5(b).

As shown in Fig. 5(b), prior to $t=15$ s, the wind speed v_w remains at 3 m/s, and the WT operates in constant low-speed mode, with an output power P_g of 0.05 p.u., a rotor speed ω_r of 0.6 p.u., and a torque T_e of 0.1 p.u. At $t=15$ s, v_w begins to rise at a rate of 1.0 m/s until it reaches 10 m/s. Between $t=15$ s and $t=20$ s, the WT operates in MPPT mode, during which both ω_r and T_e increase, and consequently increasing P_g until ω_r reaches 1.0 p.u. at $t=20$ s, signifying the entry of WT into mode III, i.e., the constant high-speed mode. At this point, because P_g is 0.9 p.u. and is less than the rated value, the pitch angle β remains at 0. However, as v_w rapidly increases to 10 m/s by $t=22$ s, P_g reaches 1.0 p.u. and the wind turbine's captured power P_{wt} exceeds 1.0 p.u. Consequently, pitch angle control is activated, which gradually increases it to 1.9°. At this condition, P_{wt} equals P_g at 1.0 p.u., and the WT operates in constant power mode. The simulation waveforms in Fig. 5(b) show well-controlled electromagnetic torque, rotor speed, and output power of the WT across all four operating modes, without any large transients, thus thoroughly validating the effectiveness of the proposed seamless speed transition control strategy.

Finally, as observed from Figs. 5(a) and (b), throughout the entire operational process of the step change and slope variation in the wind speed, u_{dc} consistently aligns with f_g, remaining stable at 1 p.u. This indicates that the seamless speed transition control strategy proposed in this paper does not affect the characteristics of DC voltage mapping to the grid frequency.

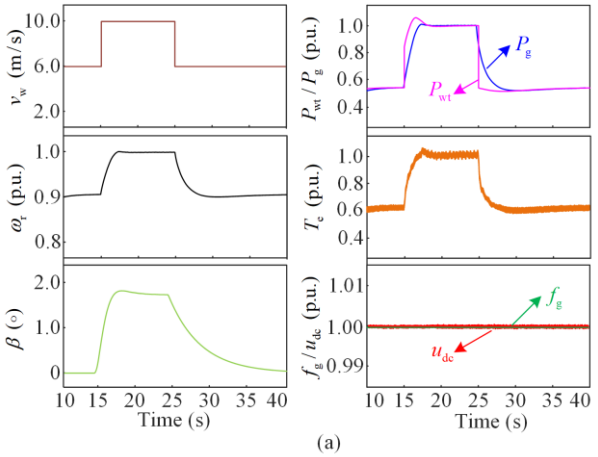

(a)

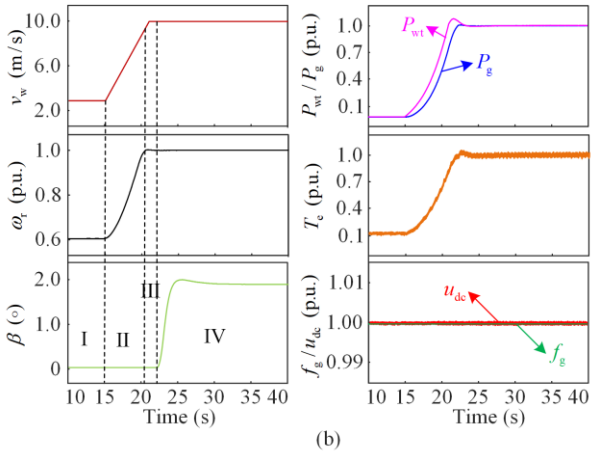

(b)

Fig. 5. Response waveforms of the IsynC-based WT during wind speed variations. (a) Wind speed step change. (b) Wind speed slope variation.

B. Verification of Adaptive Inertia Response Control

1) Case I: Operation in Low-constant-speed Mode

v_w is set to 3 m/s, while K_C is selected as 5 and 10, respectively. At $t=5$ s, the grid frequency f_g decreases at a rate of 0.005 p.u./s to 0.98 p.u., and then, at $t=15$ s, it recovers to the rated frequency at the same rate. The corresponding simulation waveforms are shown in Fig. 6, where Figs. 6(a) and (b) represent the scenarios with the K_C values of 5 and 10, respectively.

At $t=5$ s, u_{dc} follows the change in the grid frequency, maintaining its synchronization. ω_r remains at 0.6 p.u., with its active power output P_g at zero. At $t=15$ s, when the grid frequency increases, for $K_C=5$ in Fig. 6(a), ω_r increases from 0.60 p.u. to 0.62 p.u., and P_g changes from 0.05 p.u. to –0.2 p.u. For $K_C=10$ in Fig. 6(b), ω_r increases from 0.60 p.u. to 0.65 p.u., and P_g changes from 0.05 p.u. to –0.1 p.u.

The simulation results demonstrate that during the constant low-speed operation mode of the WT, when the grid frequency drops, the unit does not participate in inertia response. However, when the grid frequency increases, the rotor speed increases, storing kinetic energy, indicating the WT's capability to absorb power from the grid for inertia response.

2) Case II: Operation in MPPT Mode

v_w is set to 6 m/s, and the settings for K_C and f_g changes are the same as those in Case I. The simulation waveforms corresponding to these changes are shown in Fig. 6.

At $t=5$ s, when f_g decreases with a RoCoF of 0.01 p.u./s, u_{dc} instantly decreases by 0.01 p.u. At $K_C=5$, ω_r decreases from 0.90 p.u. to 0.885 p.u., and P_g changes from 0.5 p.u. to 0.6 p.u. For the larger K_C of 10, ω_r decreases from 0.9 p.u. to 0.7 p.u., and P_g changes

from 0.5 p.u. to 0.7 p.u. At $t=15$ s, when f_g recovers, for $K_C=5$, ω_r increases from 0.90 p.u. to 0.915 p.u., and P_g changes from 0.5 p.u. to 0.4 p.u. For $K_C=10$, ω_r increases from 0.90 p.u. to 0.93 p.u., while P_g changes from 0.5 p.u. to 0.3 p.u.

The simulation findings show that throughout the MPPT mode, a decrease in the grid frequency causes the WT to decrease its velocity, thereby extracting kinetic energy from the rotor. This suggests that the unit can effectively provide power for the inertia response. Conversely, when the grid frequency increases, the wind turbine's speed increases to store kinetic energy.

3) Case III: High-constant-speed/Constant-power Mode Operation

Given that the constant-power mode mainly relies on the action of the pitch control and that the rotation speed remains at the maximum limit, such as in the constant high-speed mode, these two scenarios will be discussed together.

v_w is 8 m/s, and the settings for the changes in K_C and f_g are the same as those in Case I. At $t=5$ s, f_g decreases from 1.0 p.u. to 0.98 p.u., while at $t=15$ s, f_g returns to its nominal value of 1.0 p.u. The corresponding simulation waveforms are shown in Fig. 6.

The WT operates at its rated speed, and P_g reaches the maximum value, positioning the unit in the constant high-speed operation mode. At $t=5$ s, as f_g decreases, u_{dc} promptly diminishes by 0.02 p.u., synchronizing with the former change. When $K_C=5$, ω_r transitions from 1.0 p.u. to 0.99 p.u., and P_g shifts from 0.9 p.u. to 1.0 p.u. Conversely, with $K_C=10$, ω_r moves from 1.0 p.u. to 0.98 p.u., and P_g changes from 1.0 p.u. to 1.1 p.u. Upon reaching $t=15$ s as f_g is reinstated, u_{dc} continues to reflexively mirror the fluctuations in the grid frequency. However, both the rotor speed and power output remain stable.

The waveforms show that during the constant high-speed operation phase, as the grid frequency decreases, the rotor decelerates, dispensing its kinetic energy and endowing the unit with the capability to extract power for the inertia response. However, when the grid frequency increases, the system refrains from the inertia response.

Moreover, in both Figs. 6(a) and (b), the variations in u_{dc} are completely consistent with those in f_g, demonstrating that changes in the K_C coefficient do not affect the mapping relationship between the DC voltage and grid frequency in the IsynC.

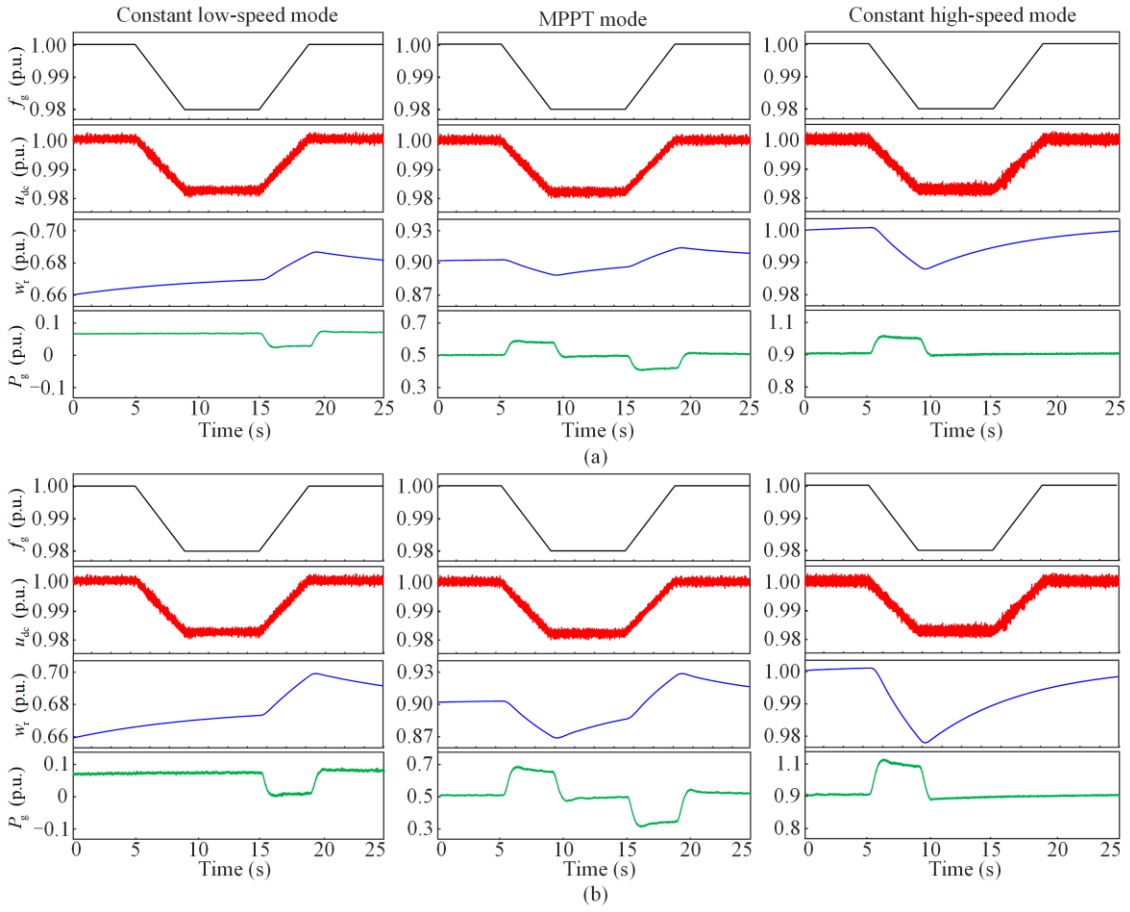

Fig. 6. Inertia response waveform of the WT under different wind speeds. (a) $K_C=5$. (b) $K_C=10$.

C. Verification of Enhanced Control in Wind Farm

To validate the efficacy of the enhanced inertia response control method proposed in this paper when multiple units operate in parallel, a model of a synchronous generator connected to a wind farm equipped with 100 grid-forming WTs is established in the PSCAD/EMTDC simulation software, as illustrated in Fig. 7.

The model shown in Fig. 7 consists of one SG (G1), four buses (Bus1–Bus4), and a grid-forming voltage source wind farm utilizing inertia-synchronization control. The fixed load and temporary load are connected via Bus2, while the wind farm is connected via Bus4. The parameters for the SG and loads are provided in Table III, and those of the WTs can be found in Table I.

TABLE III
SYNCHRONOUS GENERATOR PARAMETERS

Symbol	Description	Value
S_{SG} (GW)	Rated power of SG	1.0
R	Regulation coefficient	0.092
H (s)	Inertia time constant of SG	4.8
T_{RH} (s)	Time constant of reheater	10
F_{HP}	Power proportion of HP	0.3
S_{Lo} (MW)	Fixed load	500
S_{Tr} (MW)	Temporary load	50

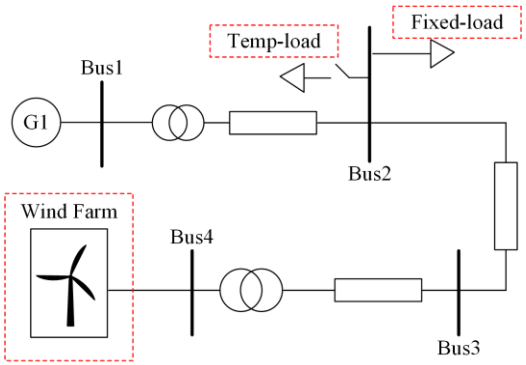

Fig. 7. Simulation model of inertia response control in the full wind speed range.

To enhance the simulation efficiency, the power equivalent aggregation method is employed, condensing the 100 WTs into 4 equivalent units with identical capacity. To validate the inertia response control in this paper, the simulation conditions are as follows.

1) Unit 1 has a wind speed of 3 m/s and operates in the constant low-speed mode with an inertia control coefficient $K_{C1}=10$.

2) Unit 2 has a wind speed of 5 m/s and functions in the MPPT mode with $K_{C2}=10$.

3) Unit 3 has a wind speed of 7 m/s and operates in the constant high-speed mode with $K_{C3}=10$.

4) Unit 4 has a wind speed of 10 m/s and functions in the constant-power region with an inertia control coefficient $K_{C4}=20$. This is used to differentiate from Mode III.

It is important to note that in reality, a more common scenario is to have different units within the same wind farm operating in three distinct states simultaneously [32], whereas having all four mentioned states concurrently present in the wind farm is an extreme case. Two simulation cases are considered here.

1) Case I: System Load Suddenly Increases by 50 MW

The corresponding simulation waveforms are illustrated in Fig. 8. Among them, $\omega_{r1}-\omega_{r4}$ represent the generator speeds of the four equivalent WT units, while $P_{g1}-P_{g4}$ signify the active power output of each unit.

Figure 8 depicts the inertia response waveforms of the units under two different control methods in the case of a sudden increase in the load. By comparison, it is evident that at $t=5$ s, when the system experienced an active power deficit, only unit 2 responds with inertia under the traditional control method in [19]. By contrast, when adopting the control method proposed in this paper, units 2, 3, and 4 all exhibit inertia responses. Moreover, each unit remains within its safe design boundaries.

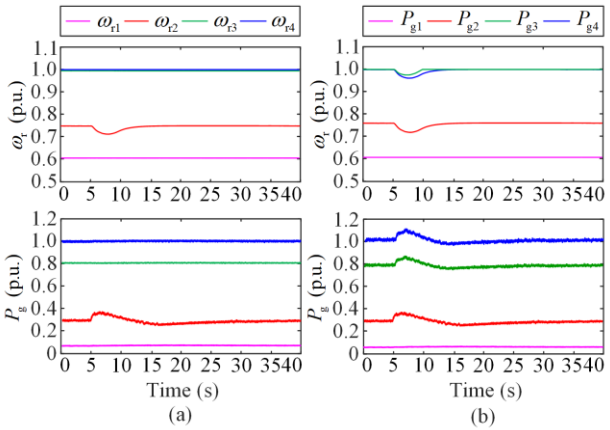

Fig. 8. Waveforms of the speed and power of the IsynC WT unit during a sudden load increase in the power system. (a) With traditional control in [19]. (b) With enhanced control.

2) Case II: System Load Suddenly Decreases by 50 MW

The corresponding simulation waveforms are illustrated in Fig. 9, which illustrates the inertia response waveforms during a sudden load decrease under two distinct control methods. It can be seen that at $t=5$ s, when the system faces an active power surplus, only unit 2 exhibits an inertia response under the conventional control approach. However, employing the proposed control strategy, both units 1 and 2 execute inertia responses.

Furthermore, Fig. 10 compares the grid frequency responses between the conventional control method and the proposed control strategy during both sudden load increase and decrease. As illustrated in Fig. 10(a), for the traditional control method, when the system load is

increased, the RoCoF is 0.161 p.u./s, with the lowest frequency value of 0.9913 p.u.. In comparison, when employing the enhanced control strategy, the RoCoF is reduced to 0.137 p.u./s, with the lowest value recorded as 0.9919 p.u. Moreover, as shown in Fig. 10(b), when the system load drops suddenly, the traditional control method in [19] results in a maximum RoCoF of 0.243 p.u./s, with the lowest frequency value of 1.0092 p.u. By contrast, the approach proposed in this paper registers a maximum RoCoF of 0.190 p.u./s and a frequency minimum of 1.0086 p.u.

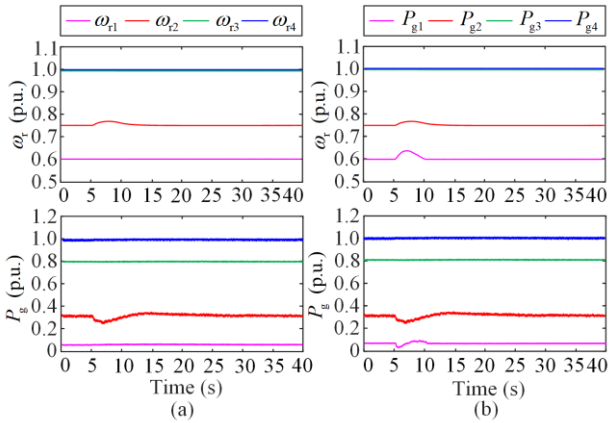

Fig. 9. Waveforms of the speed and power of the IsynC WT unit during a sudden load decrease in the power system. (a) With traditional control in [19]. (b) With enhanced control.

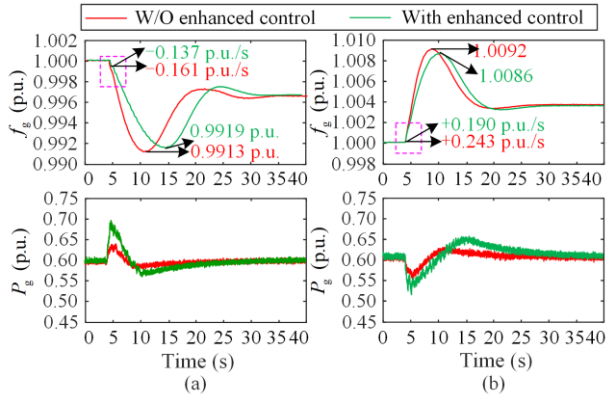

Fig. 10. Grid frequency and wind farm power response waveforms. (a) Load step up. (b) Load step down.

3) Case III: K_C Changes from 0 to 15

In this case, the impact of varying the inertia response coefficient K_C on the overall output power of the wind farm is further analyzed. In the IsynC wind farm, K_C is set to the same value for all the WTs. The waveforms of the system frequency drop and the wind farm's output power under different K_C values are depicted in Figs. 11(a) and (b), respectively. All other simulation parameters remain consistent with those in Case I.

As observed from Fig. 11, with K_C of 0, the output power of the wind farm remains at 0.6 p.u., and is unresponsive to system frequency changes. However, as K_C increases to 5, 10, and 15, the maximum active power response of the IsynC wind farm to frequency changes increases to 0.64 p.u., 0.66 p.u., and 0.69 p.u., respectively. The lowest points of the system frequency are improved from 0.9906 p.u. to 0.9912 p.u., 0.9916 p.u., and 0.9918 p.u., respectively. This indicates that increasing K_C enhances the inertia response capability of the IsynC wind farm, which helps to reduce the system frequency variations and elevate the lowest frequency points.

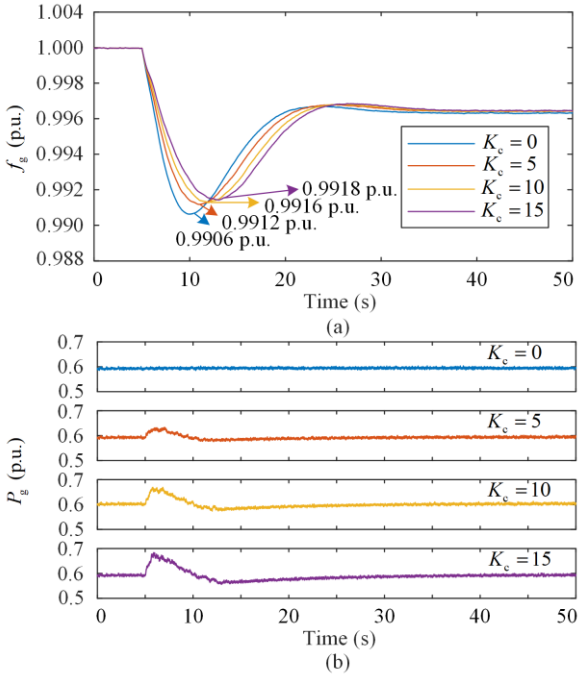

Fig. 11. Grid frequency and wind farm output power response waveforms under different K_C values.

The simulation results clearly show that, compared to the traditional method in [19], the proposed inertia response control strategy for the full wind speed range, enhances the ability of the WTs to support grid frequency. Additionally, the response power of the WTs can be adjusted by tuning the value of K_C. This improved strategy can more effectively reduce the rate of grid frequency fluctuations and lessen the extent of frequency changes.

V. Conclusion

Based on the control principle of IsynC, this paper proposes a control method that allows IsynC-controlled full-power conversion WTs to selectively participate in inertia response during all wind speed operating phases. This paper introduces an evaluation index for the inertia response performance of a WT, provides the design range and process for inertia transfer control parameters, and validates the proposed control method through simulations. The main conclusions of the study are as follows.

1) At low wind speed, the WT cannot respond to the system's positive frequency deviation with inertia. At high wind speeds, the unit does not respond to the system's negative frequency deviation with inertia. By adopting a composite judgment method based on the rate of change in the DC voltage and generator speed, selective inertia response control of the WTs throughout all wind speed ranges can be realized. This enhances the inertia response capability of the WTs. Moreover, by adjusting the inertia transfer control coefficient, the magnitude of the inertia response power can be varied.

2) The introduction of respective speed controllers in the low wind speed range and high wind speed range ensures that the regulators operate in a consistently saturated states. Setting the torque output upper limit value during the low wind speed range equal to the torque output lower limit value during the high wind speed range allows for a flexible, seamless transition between different operating regions using the desaturation effect of the PI regulators. This approach maximizes the operating range of the unit's MPPT mode.

ACKNOWLEDGMENT

Not applicable.

AUTHORS' CONTRIBUTIONS

Zhenyan Deng: full-text writing, conceptualization, and Data curation. Han Wang: revisions and funding acquisition. Yao Qin: investigation and methodology. Renxin Yang: review and editing. Xu Cai: review and construction of the paper framework. All authors read and approved the final manuscript.

FUNDING

This work is supported in part by the National Key R&D Program of China (No. 2022YFB2402703).

AVAILABILITY OF DATA AND MATERIALS

Not applicable.

DECLARATIONS

Competing interests: The authors declare that they have no known competing financial interests or personal relationships that could have appeared to influence the work reported in this article.

AUTHORS' INFORMATION

Zhenyan Deng received the B.Eng. degree in electrical engineering from Xi'an Jiao Tong University, Xi'an, China, in 2020. He is currently working toward the Ph.D. degree in electrical engineering with Shanghai Jiao Tong University, Shanghai, China. His current research interests include modeling and analysis of wind power using grid-forming control.

Han Wang received the B.Eng. degree in electrical engineering from the China University of Mining and Technology, Beijing, China, in 2005, the M.Sc. and Ph.D. degrees in electrical engineering from Shanghai Jiao Tong University, Shanghai, China, in 2008 and 2013, respectively. During 2014–2019, he was an engineer with Shanghai Mitsubishi Elevator Company, Shanghai Electric Group. During 2019–2021, he was a postdoctoral research fellow with the Department of Electrical Engineering, Shanghai Jiao Tong University. He is currently an associated professor with Wind Power Research Center, Shanghai Jiao Tong University. His research interests include high-power converters, renewable energy generation, and grid integration.

Yao Qin received the B.Eng. degree in electrical engineering and automation from the China University of Mining and Technology, Beijing, China, in 2018. He is currently working toward the Ph.D. degree in electrical engineering with Shanghai Jiao Tong University, Shanghai, China. His research focuses on the grid-forming control for wind turbine generators.

Renxin Yang received the B.Eng. degree in electrical engineering and automation from Huazhong University of Science and Technology, Wuhan, China, in 2014, and the Ph.D. degree in electrical engineering from Shanghai Jiao Tong University (SJTU), Shanghai, China, in 2020. Currently, he is a postdoctoral researcher with the Department of Electrical Engineering, SJTU. His research interests include topology, control, and fault ride-through of MMC-based HVDC system with wind farm integration.

Xu Cai received the B.Eng. degree in electrical engineering from Southeast University, Nanjing, China, in 1983, and the M.Sc. and Ph.D. degrees from the China University of Mining and Technology, in 1988 and 2000, respectively, where he was an associate professor with the Department of Electrical Engineering, from 1989 to 2001. He joined Shanghai Jiao Tong University, as a professor, in 2002, where he has been the director of the Wind Power Research Center, since2008. His research interests include power electronics and renewable energy exploitation and utilization.

REFERENCES

[1] X. Chen, A. Haddadi, and E. Farantatos *et al.*, "Power swing in systems with varying penetration of grid-forming IBRs: protection and dynamics," *Protection and Control of Modern Power Systems*, vol. 10, no. 4, pp. 116-129, Jul. 2025.

[2] L. Chen, Q. Xu, and Y. Yang *et al.*, "Community integrated energy system Trading: A comprehensive review," *Journal of Modern Power Systems and Clean Energy*, vol. 10, no. 6, pp. 1445-1458, Nov. 2022.

[3] A. Annarnraju and S. Nandiraju, "Robust frequency control in a renewable penetrated power system: an adaptive fractional order-fuzzy approach," *Protection and Control of Modern Power Systems*, vol. 4, no. 1, pp. 1-15, Jan. 2019.

[4] G. Magdy, G. Shabib and A. A. Elbaset *et al*., "Optimized coordinated control of LFC and SMES to enhance

frequency stability of a real multi-source power system considering high renewable energy penetration," *Protection and Control of Modern Power Systems*, vol. 3, no. 4, pp. 1-15, Oct. 2018.

[5] P. K. Kesavan, U. Subramaniam, and D. J. Almakhles *et al*., "Modelling and coordinated control of grid connected photovoltaic, wind turbine driven PMSG, and energy storage device for a hybrid DC/AC microgrid", *Protection and Control of Modern Power Systems*, vol. 9, no. 1, pp. 154-167, Jan. 2024.

[6] N. Nguyen and J. Mitra, "An analysis of the effects and dependency of wind power penetration on system frequency regulation," *IEEE Transactions on Sustainable Energy*, vol. 7, no. 1, Jan. 2016.

[7] M. H. El-Bahay, M. E. Lotfy, and M. A. El-Hameed, "Effective participation of wind turbines in frequency control of a two-area power system using coot optimization," *Protection and Control of Modern Power Systems*, vol. 8, no. 1, pp. 1-15, Jan. 2023.

[8] M. Kayikci and J. V. Milanovic, "Dynamic contribution of DFIG-based wind plants to system frequency disturbances," *IEEE Transactions on Power Systems*, vol. 24, no. 2, pp. 859-867, May 2009.

[9] F. Blaabjerg, R. Teodorescu, and M. Liserre *et al*., "Overview of control and grid synchronization for distributed power generation systems," *IEEE Transactions on Industrial Electronics*, vol. 53, no. 5, pp. 1398-1409, Oct. 2006.

[10] M. Arani and E. Saadany, "Implementing virtual inertia in DFIG-based wind power generation," *IEEE Transactions on Power Systems*, vol. 28, no. 2, pp. 1373-1384, May 2013.

[11] Y. Mi, B. Chen, and P. Cai *et al*., "Frequency control of a wind-diesel system based on hybrid energy storage," *Protection and Control of Modern Power Systems*, vol. 7, no. 3, pp. 1-13, Jul. 2022.

[12] G. Magdy, A. Bakeer, and M. Alhasheem, "Superconducting energy storage technology-based synthetic inertia system control to enhance frequency dynamic performance in microgrids with high renewable penetration," *Protection and Control of Modern Power Systems*, vol. 6, no. 4, pp. 1-13, Oct. 2021.

[13] L. Huang, H. Xin, and Z. Wang *et al*., "Transient stability analysis and control design of droop-controlled voltage source converters considering current limitation," *IEEE Transactions on Smart Grid*, vol. 10, no. 1, pp. 578-591, Jan. 2019.

[14] Q. Zhong and G. Weiss, "Synchronverters: inverters that mimic synchronous generators," *IEEE Transactions on Industrial Electronics*, vol. 58, no.4, pp. 1259-1267, Apr. 2011.

[15] Q. Zhong, P. Nguyen, and Z. Ma *et al*., "Self-synchronized synchronverters: inverters without a dedicated synchronization unit," *IEEE Transactions on Power Electronics*, vol. 29, no.2, pp. 617-630, Feb. 2014.

[16] L. Zhang, L. Harnefors, and H. Nee, "Power-synchronization control of grid-connected voltage-source converters," *IEEE Transactions on Power Systems*, vol. 25, no. 2, pp. 809-820, May 2010.

[17] H. Shao, X. Cai, and D. Zhou *et al*., "Equivalent modeling and comprehensive evaluation of inertia emulation control strategy for DFIG wind turbine generator," *IEEE Access*, vol. 7, pp. 64798-64811, May 2019.

[18] R. Yang, G. Shi, and C. Zhang *et al*., "Internal energy based grid-forming control for MMC-HVDC systems with wind farm integration," *IEEE Transactions on Industry Applications*, vol. 59, no. 1, pp. 503-512, Jan. 2023.

[19] S. Sang, C. Zhang, and X. Cai *et al*., "Control of a type-IV wind turbine with the capability of robust grid-synchronization and inertial response for weak grid stable operation," *IEEE Access*, vol. 7, pp. 58553-58569, May 2019.

[20] Y. Qin, H. Wang, and H. Shao *et al*., "Self-synchronization and frequency response control of PMSG-based wind turbine generator," in *IEEE 12th Energy Conversion Congress & Exposition-Asia (ECCE-Asia)*, Singapore, Singapore, May 2021, pp. 1163-1168.

[21] Y. Liu, G. Tang, and H. Liu *et al*., "Speed control method of double salient electro-magnetic wind power generator in full range of wind speed," in *2010 World Non-Grid-Connected Wind Power and Energy Conference*, Nanjing, China, Nov. 2010, pp. 1-5.

[22] A. Shafiei, B. M. Dehkordi, and A. Kiyoumarsi *et al*., "A control approach for a small-scale PMSG-based WECS in the whole wind speed range," *IEEE Transactions on Power Electronics*, vol. 32, no. 12, pp. 9117-9130, Dec. 2017.

[23] P. Li, D. Hu, and R. Hu *et al*., "Strategy for wind power plant contribution to frequency control under variable wind speed," *Renewable Energy*, vol. 130, pp. 1226-1236, Jan. 2019.

[24] J. Chen, J. Chen, and C. Gong, "New overall power control strategy for variable-speed fixed-pitch wind turbines within the whole wind velocity range," *IEEE Transactions on Industrial Electronics*, vol. 60, no. 7, pp. 2652-2660, Jul. 2013.

[25] A. Ahmed, L. Ran, and J. R. Bumby, "New constant electrical power soft-stalling control for small-scale VAWTs," *IEEE Transactions on Energy Conversion*, vol. 25, no. 4, pp. 1152-1161, Dec. 2010.

[26] H. Ye, W. Pei, and Z. Qi, "Analytical modeling of inertial and droop responses from a wind farm for short-term frequency regulation in power systems," *IEEE Transactions on Power Systems*, vol. 31, no. 5, pp. 3414-3423, Sep. 2016.

[27] Y. Wang, J. Meng, and X. Zhang *et al*., "Control of PMSG-based wind turbines for system inertial response and power oscillation damping," *IEEE Transactions on Sustainable Energy*, vol. 6, no. 2, pp. 565-574, Apr. 2015.

[28] J. N. Sakamuri, K. Das, and M. Altin *et al*., "Improved frequency control from wind power plants considering wind speed variation," in *Power Systems Computation Conference (PSCC)*, Genoa, Italy, Jun. 2016, pp. 1-7.

[29] M. Cirrincione, M. Pucci, and G. Vitale, "Neural MPPT of variable-pitch wind generators with induction machines in a wide wind speed range," *IEEE Transactions on Industry Applications*, vol. 49, no. 2, pp. 942-953, Mar. 2013.

[30] F. Jia, X. Cai, and Z. Li, "Frequency-distinct control of wind energy conversion system featuring smooth and productive power output," *IEEE Access*, vol. 6, pp. 16746-16754, Mar. 2018.

[31] R. E. K. Meesala and V. K. Thippiripati, "An improved direct torque control of three-level dual inverter fed open-ended winding induction motor drive based on modified look-up table," *IEEE Transactions on Power Electronics*, vol. 35, no. 4, pp. 3906-3917, Apr. 2020.

[32] N. Li., L. Li, and Y. Liu *et al*., "Effects of the parameter $C_{4\varepsilon}$ in the extended k-ε turbulence model for wind farm wake simulation using an actuator disc," *Journal of Marine Science and Engineering*, vol. 10, no. 4, pp. 544, Apr. 2022.